Superconducting gap symmetry from Bogoliubov quasiparticle interference analysis on Sr_2RuO_4

Shinibali Bhattacharyya,[1] Andreas Kreisel,[2] X. Kong,[3] T. Berlijn,[4]
Astrid T. Rømer,[5] Brian M. Andersen,[5] and P. J. Hirschfeld[6]

[1] *Institut für Theoretische Physik, Goethe-Universität, 60438 Frankfurt am Main, Germany*
[2] *Institut für Theoretische Physik, Universität Leipzig, D-04103 Leipzig, Germany*
[3] *Center For Nanophase Materials Sciences, Oak Ridge National Laboratory, Oak Ridge, Tennessee 37831, USA*
[4] *Center For Nanophase Materials Sciences, Oak Ridge National Laboratory, Oak Ridge, TN 37831, USA*
[5] *Niels Bohr Institute, University of Copenhagen, Rådmandsgade 62, DK-2200 Copenhagen, Denmark*
[6] *Department of Physics, University of Florida, Gainesville, Florida 32611, USA*

(Dated: June 21, 2023)

The nature of the superconducting order parameter in Sr_2RuO_4 has generated intense interest in recent years. Since the superconducting gap is very small, high resolution methods such as scanning tunneling spectroscopy might be the best chance to directly resolve the gap symmetry. Recently, a Bogoliubov quasiparticle interference imaging (BQPI) experiment has suggested that the $d_{x^2-y^2}$ gap symmetry is appropriate for Sr_2RuO_4. In this work, we use a material-specific theoretical approach based on Wannier functions of the surface of Sr_2RuO_4 to calculate the continuum density of states as detected in scanning tunneling microscopy experiments. We examine several different proposed gap order parameters, and calculate the expected BQPI pattern for each case. Comparing to the available experimental data, our results suggest that a $s' + id_{xy}$ gap order parameter is the most probable state, but the measured BQPI patterns still display features unaccounted for by the theory for any of the states currently under discussion.

I. INTRODUCTION

Sr_2RuO_4[1–4] has once again been a topic of intense research interest recently. For long time it was discussed as a promising candidate for intrinsic topological superconductor in the light of arguments in favor of a $p + ip$ symmetry of the gap order, in particular early evidence from NMR[5]. Muon-spin rotation[6] and Kerr effect[7] measurements were argued to imply time-reversal symmetry (TRS) breaking[8] in the superconducting state, consistent with this picture. However, a number of thermodynamic measurements detected low-energy quasiparticle states, hinting at the existence of nodes or deep minima in the gap $\Delta(\mathbf{k})$[9–12].

Recently, strong evidence against the chiral p-wave paradigm was provided by in-plane ^{17}O nuclear magnetic resonance measurements[13,14] that found a substantial drop in the Knight shift below T_c. Arguments in favor of spin-singlet pairing were then drawn from the field dependence of the Knight shift in comparison to the change of the entropy from earlier specific heat experiments[15]. These measurements are complemented by observations of shifts in the elastic constants[16,17] together with experiments under strain[18] that indicate a two component nature of the order parameter. All these findings have led to a series of recent theoretical attacks on the question of superconductivity in Sr_2RuO_4[19–35].

Sr_2RuO_4 is generally considered to be an unconventional superconductor, where electron pairing is mediated by the exchange of electronic excitations, so theories typically attempt to model the low-energy effective pairing interaction. The Fermi surface is dominated by three Ru d orbitals d_{xz}, d_{yz} that contribute mostly to quasi-1D bands, and d_{xy} states dominating a 2D band. Electrons in these states interact via intrasite Coulomb U interactions and Hund's coupling J, with the d_{xy} dominant bands thought to be more strongly correlated.[36,37] In addition, spin-orbit coupling plays a significant role[38,39]. Recent microscopic theories incorporate many of these ingredients[19–21,23–26,29,30,32,33,40,41], leading to a variety of predictions for $\Delta(\mathbf{k})$ depending on the assumed model and the applied methodology. These calculations point to a number of leading candidates which currently consist of the even-parity 1D irreducible representation $B_{1g}(d_{x^2-y^2})$, multi-component orders such as $d_{x^2-y^2} + ig_{xy(x^2-y^2)}$ and $s' + id_{xy}$, as well as the 2D irreducible representation $E_{1g}(d_{xz} + id_{yz})$. A two-component state is generally thought to be important to explain the observation of time-reversal symmetry breaking, ultrasound[17,42], and recent μSR experiments under strain[18]. At zero strain, these can correspond either to the 2D representation, or to accidental degeneracies of two 1D representations.

Not all such proposals are consistent with existing experimental results, nor are all the interpretations of the experimental literature apparently consistent with one another[4]. In such a situation it would be very useful to have a direct measurement of the superconducting gap to distinguish among theories and thereby constrain the possible pairing mechanisms. The tiny size ($|\Delta| \leq 350\,\mu$eV)[43,44] of the superconducting order parameter $\Delta(\mathbf{k})$ in Sr_2RuO_4 has hindered such measurements for a long time, as they require low temperatures and fine energy resolution to detect spectral features arising from the small gap. However, in principle Bogoliubov quasiparticle interference (BQPI) imaging is

a powerful technique capable of high-precision measurement of multiband $\Delta(\mathbf{k})$[45–48]. Interference of impurity-scattered quasiparticles produces real space Friedel oscillations in the density of states (DOS) $\rho(\mathbf{r},\omega)$ within the energy range of $\Delta(\mathbf{k})$, giving rise to complex patterns in the spatial Fourier transform spectrum $\rho(\mathbf{q},\omega)$ that can in principle be measured in an STM experiment and interpreted in order to extract the gap structure. The BQPI technique was recently implemented to analyze $\Delta(\mathbf{k})$ in Sr_2RuO_4[44]. This analysis, motivated with observations from recent work[12,13,19–21,49], suggested a $d_{x^2-y^2}$ superconducting gap symmetry for Sr_2RuO_4 by comparison with theoretical calculations of $\rho(\mathbf{q},\omega)$ using simple low-harmonic gap candidates $\Delta(\mathbf{k})$. Such an approach is, however, limited by a) loss of $\mathbf{q}$ space resolution when calculating BQPI on a simple Ru lattice system and b) failure to include the rather complex gap structures, including accidental nodes, anticipated by microscopic theories[19,29,33].

In this work, we will adopt the Wannier-based T-matrix technique introduced in Refs. 50 and 51 through which one obtains BQPI images for real materials in its normal and superconducting states, that are directly comparable to experiments. Unlike the theoretical approach used in Ref. 44 to obtain lattice DOS $\rho(\mathbf{R},\omega)$, the Wannier-based T-matrix approach is used for evaluation of the continuum DOS $\rho(\mathbf{r},\omega)$ dressed by real-space Wannier functions pertaining to the orbitals that have dominant contribution around the Fermi level of the material under consideration. These Wannier functions substantially modify the continuum DOS patterns, bringing in additional $\mathbf{q}(\omega)$ features in its Fourier transformed image. In addition, we take as representative of the various possible gap symmetries not only simple harmonics, but gaps derived from microscopic spin fluctuation pairing theory[29]. We find that definitive conclusions are difficult because of limited experimental tunneling spectra exhibiting superconductivity on the surface (i.e. with evidence of low-energy coherence peaks), and the fact that BQPI features are remarkably nondispersive in this system, even for highly anisotropic gap structures. The best fit to the data currently available[44] suggests a $s'+id_{xy}$ gap order parameter, but we discuss other alternatives in detail.

This paper is organized as follows: in Sec II, we introduce the multiorbital Hubbard Hamiltonian with the pairing and impurity terms, and describe it using the Bardeen-Cooper-Schrieffer (BCS) equations in the Nambu spinor basis. We write down the equations for computing the lattice DOS and continuum DOS[50,51], in the presence of impurities using the T-matrix approach. In Sec III, we demonstrate our BQPI findings first in the normal state, and second in the superconducting state of the material for which we borrow the singlet and composite gap order parameters as obtained in Refs. 19 and 29. Finally, we present our conclusions in Sec IV and possible future directions of investigation in this context.

II. MODEL

In this section, we will lay out the theoretical framework on how the surface of a material is imaged by STM. The full Hamiltonian has four terms, namely the kinetic energy term H_0, the spin-orbit term $H_{\rm soc}$, the BCS mean-field term $H_{\rm MF}$ and a single-impurity term $H_{\rm imp}$.

$$\begin{aligned} H &= H_0 + H_{\rm soc} + H_{\rm MF} + H_{\rm imp}, \qquad (1)\\ H_0 &= \sum_{\mathbf{R}\mathbf{R}'mns} t^{mn}_{\mathbf{R}\mathbf{R}'} c^\dagger_{\mathbf{R}ms} c_{\mathbf{R}'ns} - \mu_0 \sum_{\mathbf{R}ms} c^\dagger_{\mathbf{R}ms} c_{\mathbf{R}ms},\\ H_{\rm MF} &= -\sum_{\mathbf{R}\mathbf{R}'mn} [\Delta^{mn}_{\mathbf{R}\mathbf{R}'} c^\dagger_{\mathbf{R}m\uparrow} c^\dagger_{\mathbf{R}'n\downarrow} + h.c.],\\ H_{\rm imp} &= \sum_{\mathbf{R}^\star mns} V^{mn}_{\rm imp} c^\dagger_{\mathbf{R}^\star ms} c_{\mathbf{R}^\star ns}. \end{aligned}$$

$H_{\rm soc}$ will be introduced in the next subsection. Here, $c^\dagger_{\mathbf{R}ms}$ ($c_{\mathbf{R}ms}$) is the creation (annihilation) operator for an electron in the unit cell $\mathbf{R}$, orbital m with spin s. $t^{mn}_{\mathbf{R}\mathbf{R}'}$ is the amplitude for hopping from unit cell $\mathbf{R}$, orbital m to the unit cell $\mathbf{R}'$, orbital n. The pairing field is given by $\Delta^{mn}_{\mathbf{R}\mathbf{R}'} = V^{mn}_{\mathbf{R}\mathbf{R}'} \langle c_{\mathbf{R}'n\downarrow} c_{\mathbf{R}m\uparrow}\rangle$, where $V^{mn}_{\mathbf{R}\mathbf{R}'}$ is the effective attraction between unit cell $\mathbf{R}$, orbital m and unit cell $\mathbf{R}'$, orbital n. $\mathbf{R}^\star$ is the impurity site and $V^{mn}_{\rm imp}$ is the (on-site only) non-magnetic impurity potential responsible for scattering of quasiparticles.

A. Non-interacting Hamiltonian

We will adopt the non-interacting tight-binding Hamiltonian model for Sr_2RuO_4 as used in Refs. 19, 27, and 29. It is composed of the three Ru orbitals: d_{xz}, d_{yz} and d_{xy}. Fourier transforming the real space hoppings from H_0 fitted to ARPES measurements[52,53], one obtains the dispersions given by $\xi_{xz}(\mathbf{k}) = -2t_1\cos k_x - 2t_2\cos k_y - \mu$, $\xi_{yz}(\mathbf{k}) = -2t_2\cos k_x - 2t_1\cos k_y - \mu$, and $\xi_{xy}(\mathbf{k}) = -2t_3(\cos k_x + \cos k_y) - 4t_4\cos k_x\cos k_y - 2t_5(\cos 2k_x + \cos 2k_y) - \mu$ with $\{t_1,t_2,t_3,t_4,t_5\} = \{88,9,80,40,5,109\}$ meV with the inter-orbital hybridization $g(\mathbf{k})$ set to 0 (see Eq. (2) below) and the chemical potential $\mu = 109$ meV. Atomic SOC is parametrized by $H_{\rm soc} = \lambda_{\rm soc}\mathbf{L}\cdot\mathbf{S}$ and gives rise to orbital mixing on the Fermi surface sheets. We include SOC of $\lambda_{\rm soc} \approx 40$ meV ($\approx 0.5t_1$)[19,27,29]. For the TRS-preserved normal state, we have doubly degenerate Kramer's eigenvalues and the non-interacting Hamiltonian $\hat{H}$ in block-diagonal form can be represented in a pseudospin basis $\sigma = +(-)$. Here $\hat{H} = \sum_{\mathbf{k}\sigma}\Psi^\dagger(\mathbf{k},\sigma)(H_0 + H_{\rm soc}(\sigma))\Psi(\mathbf{k},\sigma)$ where,

$$H_0 = \begin{pmatrix} \xi_{xz}(\mathbf{k}) & g(\mathbf{k}) & 0\\ g(\mathbf{k}) & \xi_{yz}(\mathbf{k}) & 0\\ 0 & 0 & \xi_{xy}(\mathbf{k}) \end{pmatrix}, \qquad (2)$$

$$H_{\rm soc}(\sigma) = \frac{1}{2}\begin{pmatrix} 0 & -i\sigma\lambda_{\rm soc} & i\lambda_{\rm soc}\\ i\sigma\lambda_{\rm soc} & 0 & -\sigma\lambda_{\rm soc}\\ -i\lambda_{\rm soc} & -\sigma\lambda_{\rm soc} & 0 \end{pmatrix}, \qquad (3)$$

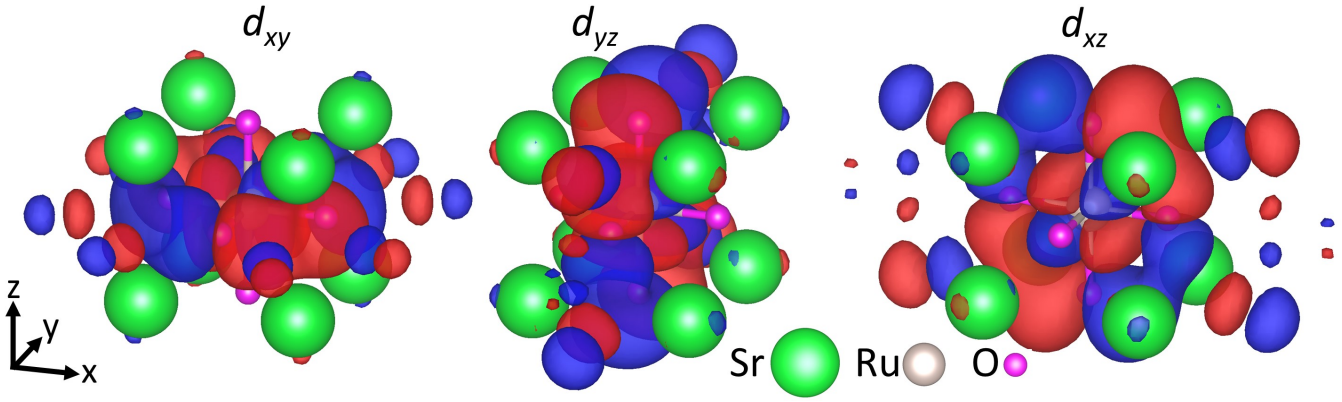

FIG. 1. Isosurface plots of Ru d_{xy}, d_{yz} and d_{xz} Wannier orbitals in Sr_2RuO_4. The atoms Sr, Ru and O are depicted by the opaque spheres colored in green, white and pink, respectively. The Ru atom is positioned at the center of the unit cell which has an in-plane lattice constant of $a = 3.8644$ Å as considered in the *ab-initio* calculations described in Appendix A. The Wannier functions are depicted by the translucent red and blue colored lobes indicating opposite phases of the wave functions.

and $\Psi(\mathbf{k},+) = [c_{xz\uparrow}(\mathbf{k}), c_{yz\uparrow}(\mathbf{k}), c_{xy\downarrow}(\mathbf{k})]^T$ and $\Psi(\mathbf{k},-) = [c_{xz\downarrow}(\mathbf{k}), c_{yz\downarrow}(\mathbf{k}), c_{xy\uparrow}(\mathbf{k})]^T$.

B. Superconducting gap

The full BCS Hamiltonian (implied by the underscore) is given by:

$$\underline{\hat{H}} = \begin{pmatrix} \hat{H}(\mathbf{k}) & \hat{\Delta}(\mathbf{k}) \\ \hat{\Delta}^\dagger(\mathbf{k}) & -\hat{H}^T(-\mathbf{k}) \end{pmatrix}, \tag{4}$$

written in the Nambu spinor basis $(\Phi^\dagger(\mathbf{k}), \Phi^T(-\mathbf{k}))$ where $\Phi^\dagger(\mathbf{k}) = (\Psi^\dagger(\mathbf{k},+), \Psi^\dagger(\mathbf{k},-))$. The superconducting gap in momentum space in the homogeneous system $\hat{\Delta}(\mathbf{k})$ is obtained from the spin-fluctuation pairing theory evaluations[19,29]. Diagonalizing $\underline{\hat{H}}$ yields the eigenvalues $\{\pm E_\mu(\mathbf{k})\}$ and the unitary transformation matrix $\underline{\hat{U}}(\mathbf{k})$ that diagonalizes $\underline{\hat{H}}$. The orbitally resolved-gap structure $\hat{\Delta}^{mn}(\mathbf{k})$ is also expressed in this Nambu basis[51] [see Appendix B for theoretical details]. We evaluate six different cases of pseudospin-singlet $(|\uparrow\downarrow\rangle - |\downarrow\uparrow\rangle)$ gap order parameters: simple intra-band $d^S_{x^2-y^2}$ where $\hat{\Delta}_\mu(\mathbf{k}) = \frac{\Delta_0}{2}(\cos k_x - \cos k_y)$, and the rest taken from Refs. 19 and 29 $d_{x^2-y^2}$, s', $s' + id_{x^2-y^2}$ and $s' + id_{xy}$. The spin-fluctuation mediated pairing theory for weakly-coupled systems (like Sr_2RuO_4) enables one to find the phase diagram of the possible leading gap order parameters as a function of the on-site Coulomb repulsion U and Hund´s coupling J interaction terms [19]. The gap solutions $d_{x^2-y^2}$, s' and $s' + id_{x^2-y^2}$ are the results of such an analysis pertaining to different U and J values. Furthermore, Ref. 29 also included the effect of nearest-neighbor Coulomb repulsion V to investigate the fate of the leading gap order which yields a robust $s' + id_{xy}$ solution.

The orbitally-resolved homogeneous DOS in the superconducting state is $\rho^n(\omega) = -\frac{1}{\pi}\mathrm{Im}\sum_{\mathbf{k}} \hat{G}_{nn}(\mathbf{k},\omega)$ where

$$\underline{\hat{G}}(\mathbf{k},\omega) = (\omega - \underline{\hat{H}}(\mathbf{k}) + i\delta)^{-1}, \tag{5}$$

is the Green's function for the BCS Hamiltonian. The real-space bare lattice Green's function is obtained from the Fourier transform

$$\underline{\hat{G}}^0(\mathbf{R},\mathbf{R}',\omega) = \sum_{\mathbf{k}} e^{-i\mathbf{k}.(\mathbf{R}-\mathbf{R}')}\underline{\hat{G}}^0(\mathbf{k},\omega) = \underline{\hat{G}}^0(\mathbf{R}-\mathbf{R}',\omega). \tag{6}$$

C. Impurity states and T-matrix approach

With intra-orbital, on-site impurity potential terms V^{nn}_{imp} in H_{imp} of Eq. (1), one constructs the lattice Green's function in the presence of the impurity via the T-matrix approach:

$$\underline{\hat{G}}(\mathbf{R},\mathbf{R}',\omega) = \underline{\hat{G}}^0(\mathbf{R}-\mathbf{R}',\omega) + \underline{\hat{G}}^0(\mathbf{R},\omega)\underline{\hat{T}}(\omega)\underline{\hat{G}}^0(-\mathbf{R}',\omega). \tag{7}$$

The T-matrix is given by

$$\underline{\hat{T}}(\omega) = [\mathbb{1} - \underline{\hat{V}}_{\mathrm{imp}}\underline{\hat{G}}(\omega)]^{-1}\underline{\hat{V}}_{\mathrm{imp}}, \tag{8}$$

where the local Green's function is $\underline{\hat{G}}(\omega) = \sum_{\mathbf{k}} \underline{\hat{G}}(\mathbf{k},\omega)$ and the diagonal matrix $\underline{\hat{V}}_{\mathrm{imp}} = V^{mn}_{\mathrm{imp}}\delta_{mn}\underline{\tau_z}$, implying its expression in the Nambu spinor basis with

$$\underline{\tau_z} = \begin{pmatrix} \mathbb{1} & 0 \\ 0 & -\mathbb{1} \end{pmatrix}. \tag{9}$$

D. Wannier functions to calculate continuum density of states

For a given bias voltage V, the differential tunneling conductance in an STM experiment is given by[54]:

$$\frac{dI}{dV}(\mathbf{r}, eV) = \frac{4\pi e}{\hbar}|M|^2\rho_{\mathrm{tip}}(0)\rho(\mathbf{r}, eV), \tag{10}$$

where $\mathbf{r} = (x, y, z)$ denote the coordinates of the tip, $\rho(\mathbf{r}, eV)$ is the continuum LDOS (cLDOS), $\rho_{\rm tip}(0)$ is the DOS of the tip, and $|M|^2$ is the square of the matrix element for the tunneling barrier. The following methodology to include the effect of Wannier functions in modifying the cLDOS was introduced in Refs. 50 and 51. The cLDOS can be calculated by

$$\rho(\mathbf{r}, \omega) = -\frac{1}{\pi} \mathrm{Im} G^{11}(\mathbf{r}, \mathbf{r}, \omega), \tag{11}$$

where $G^{11}(\mathbf{r}, \mathbf{r}, \omega) = \sum_s G_{ss}(\mathbf{r}, \mathbf{r}, \omega)$ is the normal part of the Nambu continuum Green's function defined in a basis described by the field operators $\psi_s(\mathbf{r})$. These are related to the lattice operators $c_{\mathbf{R}ms}$ through the Wannier functions matrix elements $w_{\mathbf{R}m}(\mathbf{r})$ as $\psi_s(\mathbf{r}) = \sum_{\mathbf{R}m} c_{\mathbf{R}ms} w_{\mathbf{R}m}(\mathbf{r})$. Employing the Wannier basis transformation[50,51], we can obtain the continuum Green's function as:

$$G_{ss'}(\mathbf{r}, \mathbf{r}', \omega) = \sum_{\mathbf{R}\mathbf{R}'mn} \hat{G}_{ms,ns'}(\mathbf{R}, \mathbf{R}', \omega) w_{\mathbf{R}m}(\mathbf{r}) w_{\mathbf{R}'n}(\mathbf{r}') \tag{12}$$

and thereafter, evaluate the cLDOS from Eq. (11). A simple Fourier transform of the cLDOS $\rho(\mathbf{r}, \omega)$ gives the Bogoliubov quasiparticle interference maps that can be compared directly to experimental measurements.

III. RESULTS

The Sr_2RuO_4 crystal structure is composed of alternating layers of SrO and RuO_2 planes. The cleaving of the sample in ultrahigh vacuum at low temperatures is considered to reveal atomically flat SrO cleaved surface[44]. However, an STM tip probing this surface is believed to be sensitive to the atomic wave functions of the Ru $d-$orbitals that dominate the Fermi level, while the other atomic wave functions away from the Fermi level are effectively invisible for STM. An illustration of the Ru $d-$orbitals Wannier functions [as obtained from *ab-initio* calculations described in Appendix A] is provided in Fig. 1. Notice the smaller z-expanse of the d_{xy} Wannier orbitals compared to d_{xz}, d_{yz} orbitals, making d_{xy} orbital less likely to participate in tunneling through an STM tip located at a certain $z-$height above the cleaved surface. This property might be altered on reconstructed surfaces[55]; in this work we concentrate on the spectroscopic features at low energies assuming no reconstruction and a negligible effect from the van Hove singularities. Whether these effects are essential for the observation of superconductivity in Sr_2RuO_4 is not presently clear, as the presence or absence of reconstruction is not always examined in the experimental data[43,44].

A. Homogeneous superconducting state

Figure 2(a) shows the Fermi surface (FS) for 2D Sr_2RuO_4 with the corresponding dominant orbital contribution. There are three FS pockets: two quasi-1D bands that originate from Ru d_{xz} (purple) and d_{yz} (yellow) orbitals, leading to the electron-like β band centered at the Γ point and hole-like α band surrounding the M point; and the Ru d_{xy} (blue) orbital generates the electron-like quasi-2D γ band centered at the Γ point. SOC lifts degeneracy of the β and γ bands along the diagonals in the first Brillouin zone (BZ) and introduces further inter-orbital hybridization as seen in Fig. 2(a).

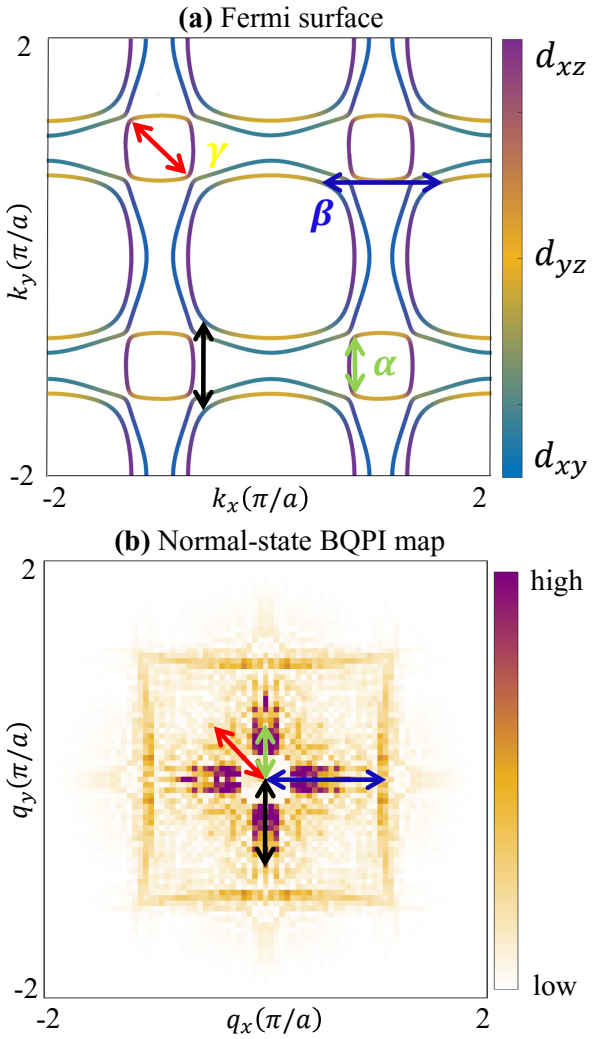

FIG. 2. (a) Fermi surface of Sr_2RuO_4 for the model discussed in Sec.II A with patches showing the dominant orbital content (d_{xz}, d_{yz} or d_{xy}) as indicated by the color legend. The normal state intra-band scattering vectors connecting patches with similar orbital character are indicated by red, green, black and blue arrows. (b) The QPI pattern for an impurity potential $V_{\rm imp} = 0.05$ eV and for $\omega = 0$ eV in the normal state of the system. The $\mathbf{q}$-vectors corresponding to these red, green, black and blue arrows as shown in (a) are highlighted as well. Intensities in the central region surrounding $\mathbf{q} = (0, 0)$ have been suppressed for visual clarity.

Figure 3 shows the orbitally-resolved homogeneous DOS $\rho^n(\omega)$ in the superconducting state, with degener-

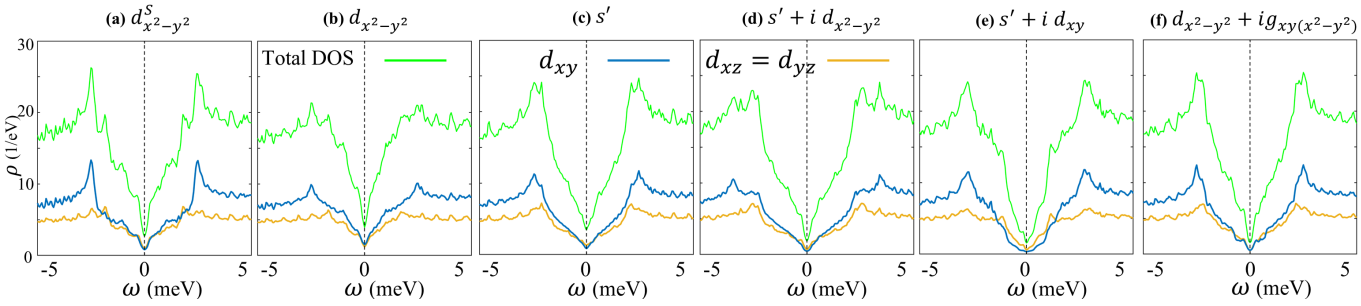

FIG. 3. Homogeneous orbitally-resolved DOS in the superconducting state for six different gap order parameters: (a) $d^S_{x^2-y^2}$ which is a simple intra-band order parameter of $\frac{\Delta_0}{2}(\cos k_x - \cos k_y)$, and the rest taken from Refs. 19 and 29 (b) $d_{x^2-y^2}$, (c) s', (d) $s' + id_{x^2-y^2}$, (e) $s' + id_{xy}$ and (f) $d_{x^2-y^2} + ig_{xy(x^2-y^2)}$. Notice the V-shaped DOS spectrum across all cases.

ate contributions from d_{xz} and d_{yz} orbitals depicted by the dark-yellow line and d_{xy} orbital contribution in blue. Results are presented for six different pseudospin-singlet gap order parameters: (a) purely intra-band $d^S_{x^2-y^2} = \frac{\Delta_0}{2}(\cos k_x - \cos k_y)$ (the superscript 'S' denotes the simple cosine form of the order parameter), and the rest adapted from Refs. 19 and 29 (b) $d_{x^2-y^2}$, (c) s', (d) $s' + id_{x^2-y^2}$, (e) $s' + id_{xy}$ and (f) $d_{x^2-y^2} + ig_{xy(x^2-y^2)}$. While the gap functions (b)-(f) correspond to specific cases of microscopic parameters discussed in those references, it was shown there that their structure was reasonably robust against changes of those parameters within reasonable ranges. Thus we hope therefore to identify qualitative BQPI structures that are driven by these features. Case (a) with $d^S_{x^2-y^2}$ order parameter was evaluated to compare directly with the BQPI analysis claims of Ref. 44. The gap maximum value for all cases was chosen as $\Delta_0 = 3.5$ meV, as required with the **k**-grid size employed. A lower value of Δ_0 would require a larger **k**-grid size for converged calculations; we verified that the qualitative features of computed BQPI patterns were robust against changes in the **k**-grid.

The gap functions studied here all possess nodes or extremely deep near-nodes on the Fermi surface[19,29], such that spectra in Fig. 3 are all roughly V-shaped, consistent with STM measurements[44,56]. Certain small features related to the multiband character of Sr_2RuO_4 are clearly visible, however. One can clearly identify the coherence peaks appearing in the vicinity of $\Delta_0 = \pm 3.5$ meV. Although some cases, particularly (e) with $s' + id_{xy}$ order parameter, show evidence of shoulders in the DOS at energies less than Δ_0, this is not captured in experiments possibly due to: (1) the extremely low STM-bias resolution required to differentiate such a feature occurring below $\pm 350\,\mu$eV in the real system, and (2) smoothing of the DOS spectrum due to convolution with Fermi distribution function at finite temperatures as measured in the dI/dV spectrum[54]. We have used 1000×1000 **k**-grid and a broadening parameter of 0.1 meV for the above calculations.

B. Inhomogeneous superconducting state

To consider scattering from a single point-like impurity, we introduce an impurity substituting one of the atoms in the center of the cleaved surface and calculate the cLDOS over an area of 51×51 lattice constants. We consider a weak non-magnetic impurity scatterer (Born limit) that is purely intra-orbital, and diagonal in spin space, i.e. $(V^{nn}_{\rm imp})_{ss} = 0.05$ eV appearing in Eq. (8). Modeling the disorder is the most uncertain part of this analysis, since we do not have microscopic knowledge of the sources of scattering. We therefore follow the simplest path by modeling impurities by a single δ-function with a potential chosen to best reproduce the simpler normal state QPI pattern. Thus, here we do not consider various forms of dressed impurity potentials arising from electronic correlations[57–66]. We evaluate the Wannier function-modified cLDOS pattern obtained from Eq. (11), first, for the normal state and next, for the superconducting states discussed under cases (a-f) in Sec.III A. The spatial cLDOS is calculated on the xy-plane at a specific z-height above the cleaved surface of the sample (here, $z = 4.93$Å is used for the Wannier functions). The specific choice of $V_{\rm imp}$ produces the QPI map of the normal state scattering processes at $\omega = 0$ eV as shown in Fig. 2(b) and shows qualitative agreement with experimental results of Ref.[44 and 67]. The normal state intra-band scattering vectors connecting FS patches with similar orbital character across neighboring BZ are indicated by the red, green, black and blue arrows in Fig. 2(a). These specific **q**-vectors are highlighted in Fig. 2(b) representing the normal state QPI map. The specific double-cross feature was also observed in earlier experimental work[44,67], but an interpretation of its origin was not discussed in those works. We found that most of the prominent **q**-features, including the sharp double-cross feature, arise from inter and intra-band $d_{xz/yz}$-scattering, as represented by the green, black and blue arrows. One can notice less-intense **q**-features corresponding to the suppressed tunneling matrix elements for d_{xy} orbitals along the diagonals of the BZ indicated by the red arrow (which has been shown separately

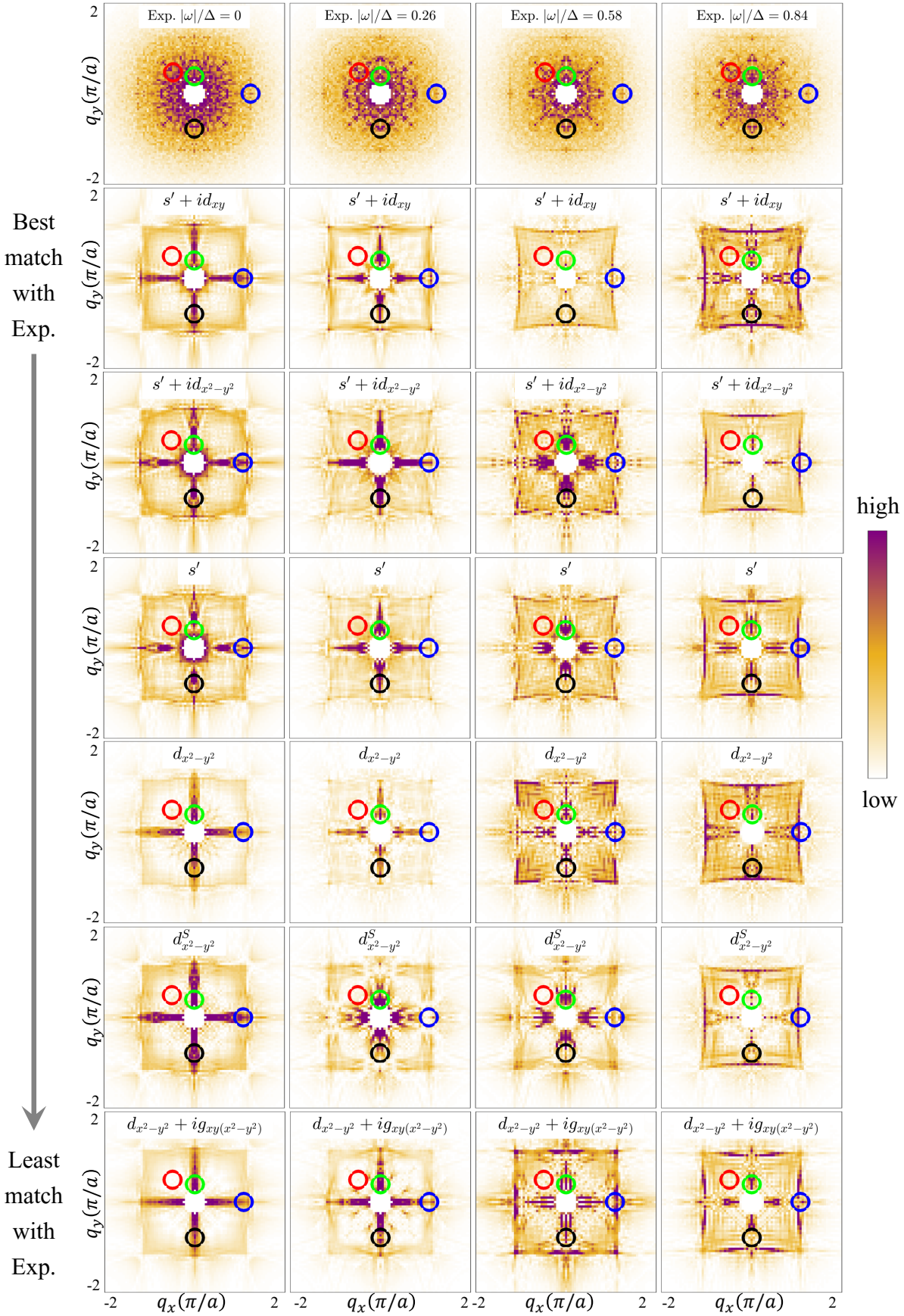

FIG. 4. BQPI maps obtained in the superconducting state from: (top row) experimental data[44] obtained at four different STM bias values $|\omega|/\Delta = [0, 0.26, 0.58, 0.84]$ as marked for each column, followed by our theoretical predictions for $s' + id_{xy}$, $s' + id_{x^2-y^2}$, s', $d_{x^2-y^2}$, $d^S_{x^2-y^2}$ and $d_{x^2-y^2} + ig_{xy(x^2-y^2)}$. The most noticeable $\mathbf{q}$-features across all bias values are encircled in red, green, blue and black. Intensities in the region surrounding $\mathbf{q} = (0, 0)$ have been suppressed for visual clarity.

in Fig. 7(b)). We have provided our detailed discussion about the $d_{xz/yz/xy}$-orbital contributions, as evidenced by the orbitally resolved normal state QPI maps, in Appendix C.

Next, we discuss the results for BQPI maps obtained in the superconducting state as shown in Fig. 4 for cases (a-f). The top row shows the experimental BQPI data[44] obtained at four different STM bias values $|\omega|$ expressed in units of the experimentally observed gap-maxima $\Delta = 350\,\mu$eV. For subsequent rows, $|\omega|$ is expressed in units of theoretically observed coherence peak values. These values correspond to: $|\omega|/\Delta = [0, 0.26, 0.58, 0.84]$. The most consistently noticeable $\mathbf{q}(\omega)$-features across all bias values are encircled in red, green, blue and black circles. Small $|\mathbf{q}|$-features in the experiments are believed to be due to long-range disorder/drift in real space rather than any scattering interference, and hence, are removed from the plots. We compared these specific features appearing in our theoretically evaluated BQPI maps corresponding to the six different singlet and composite order parameters.

Before proceeding, we note one salient aspect of the application of the BQPI technique to SRO and other low-T_c unconventional superconductors. While we have emphasized the utility of the technique to provide information on the gap structure in superconductors with low T_c, such systems often have much larger Dirac cone anisotropies $v_F/v_\Delta \sim E_F/\Delta_0$ than, e.g., cuprates or Fe-based superconductors. As can be seen in the experimental data, there is therefore virtually no dispersion of the BQPI peak positions in the superconducting state, although the weights of these peaks change with bias. Colloquially, this is because the contours of constant quasiparticle energy are arcs rather than "bananas". The dispersion takes place over a much smaller, and probably un-resolvable range of $\mathbf{q}$. An analysis based on an analog of the "octet" model applied to cuprates[68] is therefore not possible, eliminating one of the most powerful tools to identify the gap structure from BQPI.

We are therefore limited to comparing theoretical and experimental QPI maps at different biases and attempting to identify the most qualitatively robust features. In Fig. 4, we arranged the rows of BQPI maps below the experimental data (first row) in a descending order starting from the case showing the most to the least consistency with the experimental patterns, i.e., second row for $s'+id_{xy}$, third for $s'+id_{x^2-y^2}$, fourth for $d^S_{x^2-y^2}$, fifth for s', sixth for $d_{x^2-y^2}$ and seventh for $d_{x^2-y^2} + ig_{xy(x^2-y^2)}$. In other words, the BQPI pattern for $s' + id_{xy}$ order parameter shows the closest similarity at the four $\mathbf{q}$-positions of the colored circles across all bias values, whereas $d_{x^2-y^2} + ig_{xy(x^2-y^2)}$ order parameter shows the least correspondence with these four specific $\mathbf{q}$-features. These four $\mathbf{q}$-positions were first identified from their ubiquitous and robust presence across all bias values in the experimental BQPI maps, and thereafter, their corresponding presence in the theoretically predicted BQPI maps were investigated[44]. Furthermore, to quantify the similarities, we evaluated the mean-squared deviation (MSD) $\overline{\Delta y(j)}$ of the integrated intensities around the four specific $\mathbf{q}$-points across all STM bias values for different order parameters (j), weighted inversely by their extent of mismatch compared to their experimental counterparts. A summary score chart of this correspondence is quantified in Table I below and a more detailed description is given in Appendix D. Additionally, the experimental features at higher STM biases $|\omega|/\Delta = [0.58, 0.84]$ show enhanced intensities along the square edges positioned around $(\pm 1.5\pi/a)$, as opposed to the lower biases $|\omega|/\Delta = [0, 0.26]$. This trend is also observed in the BQPI maps for the $s'+id_{xy}$ and the $s'+id_{x^2-y^2}$ order parameters, whereas the other order parameters tend to exhibit this feature at other bias values, not aligning with this trend. This enhanced square feature is believed to be arising from increased scattering between gradually re-appearing normal-state-like Bogoliubov contours at higher bias values.

As discussed in Ref. 44, the $d_{xz/yz}$ dominated α, β bands are detected from the normal-state scattering interference wave-vectors (blue, green and black arrows in Fig. 2(a)) and subsequently, yield prominent signatures in the superconducting state. With the knowledge that our gap order parameter exhibits multiple nodes and/or minima in the vicinity of $(\pm\pi/a, \pm\pi/a)$ on α, β bands, there could be numerous scattering wave-vectors connecting these $\mathbf{k}$-regions. This gives rise to the rich and intricate BQPI patterns as observed in experiment and in our theoretical evaluations as well. However, we note that the most significant features highlighted by the blue, green and black circles (in Fig. 4) correspond to major scattering wave-vectors connecting the Bogoliubov contours along the $(\pm\pi/a, \pm\pi/a)$ on α and β bands. Detecting BQPI intensities along the diagonal regions of the BZ is somewhat challenging in our numerical evaluations. This is because, in our current tight-binding model together with *ab-initio* derived Wannier functions, the small value

Gap order	Weighted Mean Squared Deviation
$s'+id_{xy}$	2.79
$s'+id_{x^2-y^2}$	2.93
$d^S_{x^2-y^2}$	2.94
s'	3.07
$d_{x^2-y^2}$	3.17
$d_{x^2-y^2} + ig_{xy(x^2-y^2)}$	5.62

TABLE I. Score chart summarizing the weighted mean-squared deviation $\overline{\Delta y(j)}$ of the integrated BQPI intensity around the four specific $\mathbf{q}$-features at the colored circles (see Fig. 4) between experimental and theoretically evaluated BQPI maps, for various gap order parameters (j). The numbers are sorted starting from the least ($s'+id_{xy}$) to the highest ($d_{x^2-y^2} + ig_{xy(x^2-y^2)}$) MSD corresponding to various order parameters. This score determines the ranking for the correspondence of the individual gap order parameters when matched with experimental BQPI patterns.

of the d_{xy} Wannier function significantly suppresses the scattering matrix elements. Further details are discussed in Appendix C.

IV. SUMMARY

The question of the gap structure of Sr_2RuO_4 in momentum space is difficult to address experimentally due to the small superconducting energy scales in this system. At present, Bogoliubov quasiparticle interference measurements appear to be the only method of pinning down the location of gap nodes. We have therefore performed 2D calculations of the real-space Wannier function-modified continuum electronic density of states for Sr_2RuO_4. Using the T-matrix approach in combination with Wannier functions for analyzing scattering effects from a single impurity, we evaluated the real-space tunneling conductance map and displayed its Fourier transformed BQPI image to compare with STM measurements[44]. We have shown our evaluations for six possible pseudospin-singlet and composite gap order parameters: (a) purely intra-band $d^S_{x^2-y^2}$ parameter ($\frac{\Delta_0}{2}(\cos k_x - \cos k_y)$), and the rest borrowed from Refs. 19 and 29: (b) $d_{x^2-y^2}$, (c) s', (d) $s' + id_{x^2-y^2}$, (e) $s' + id_{xy}$, and (f) $d_{x^2-y^2} + ig_{xy(x^2-y^2)}$. We compared the important features between our theoretical predictions and the experimental measurements for the homogeneous DOS spectrum and the BQPI patterns, and concluded that the $s' + id_{xy}$ gap order parameter seems to be the most consistent with our observations. However, the analysis is at best quantitative; the overall agreement with the measured patterns does not seem sufficiently impressive at this time to make a strong case for any of the above 2D states. Since the analysis of BQPI patterns is a classic example of "pattern recognition" problem[69], future investigations in this context can be directed towards training convolutional neural networks with theoretically generated images of BQPI patterns labeled for various STM biases and gap order parameters, and testing them on experimental data sets. This will facilitate less manual interference in analyzing complicated and rich patterns in data, and will be less prone to bias and estimation errors.

ACKNOWLEDGMENTS

We thank Rahul Sharma and J.C. Davis for sharing experimental data with us and for many helpful discussions that paved the course of the analysis presented in this work. We also thank Ilya Eremin, Marvin Müller, Miguel Sulangi, Roser Valentí and Karim Zantout for useful discussions. S.B. acknowledges support from the Deutsche Forschungsgemeinschaft (DFG, German Research Foundation) through TR 288-422213477. B. M. A. and A. T. R. acknowledge support from the Independent Research Fund Denmark grant number 8021-00047B. P.J.H. and S.B. acknowledge partial support from DOE-BES DE-FG02-05ER46236. A portion of this research was conducted at the Center for Nanophase Materials Sciences, which is a DOE Office of Science User Facility (T. B., X. R. K.). This research used resources of the Compute and Data Environment for Science (CADES) at the Oak Ridge National Laboratory, which is supported by the Office of Science of the U.S. Department of Energy under Contract No. DEAC05-00OR22725.

Appendix A: First principles Wannier function calculations

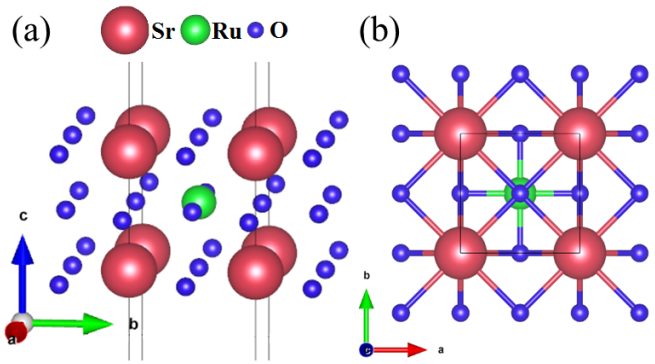

FIG. 5. (a) The cell (constituent atoms and vacuum) of Sr_2RuO_4 depicted with black borders and constituent atoms Sr (maroon), Ru (green) and O (blue) as indicated by the color legend. The upper and lower extension of the cell into vacuum has not been shown for brevity. Axis orientations are shown in the left-bottom corner. (b) Surface geometry of Sr_2RuO_4 when viewed above a certain height from the surface, with the Sr (maroon) and O (blue) atoms on very similar z-level. The bonds (in-plane and out-of-plane) between different atoms are depicted by the bi-colored lines.

The Wannier functions in this work were derived following the same procedure as in Ref. 55. In this work however, no octahedral rotations were incorporated. Therefore, we could use the Sr_2RuO_4 normal cell instead of a $\sqrt{2}\times\sqrt{2}$ $Sr_4Ru_2O_8$ supercell. As a first step, we performed Density Functional Theory (DFT) calculations of monolayer Sr_2RuO_4 with an in-plane lattice constant $a =$ 3.8644 Å and a vacuum layer of roughly 20 Å. The corresponding unit cell is depicted in Fig. 5. Including the vacuum in our calculations allowed us to simulate the Wannier functions above the surface of Sr_2RuO_4 where the STM tip resides. For the DFT calculations we employed the Vienna ab initio simulation package (VASP)[70,71]. We used the generalized gradient approximation of Perdew, Burke and Ernzerhof[72], a plane-wave energy cut-off of 650 eV and a $7 \times 7 \times 1$ k-mesh. In the second step, we derived the Wannier functions with the Wannier90 software[73]. Specifically, we projected the Ru-t_{2g} orbitals on the bands roughly within $[-9.55, 1.45]$ eV. Furthermore, we set `num_iter` $= 0$ and `dis_num_iter` $= 10000$,

and took the inner frozen energy window to be roughly equal to $[-1.65, 1.45]$ eV.

Appendix B: Representing pairing functions in orbitally-resolved Nambu basis

The gap function obtained from Refs. 19 and 29 and illustrated in Fig. 6 are expressed as a function of the normal state Fermi surface (FS) $\Delta_\mu(\mathbf{k_F})$, where the gap magnitude tends to be the largest compared to the rest of the BZ. To obtain the gap function over the full BZ as required in Eq. (4), one can extrapolate its value from the μ-th Fermi band $\Delta_\mu(\mathbf{k_F})$ as it falls off away from the FS, a behavior which can be parametrized in terms of a Gaussian-cutoff:

$$\Delta_\mu(\mathbf{k}) = \Delta_\mu(\mathbf{k_F}^{\rm nn.}) \exp\left(-\left(|E_\mu(\mathbf{k})|/\Delta_C\right)^2\right), \quad \text{(B1)}$$

where $\Delta_C = 10\Delta_0$ and $\mathbf{k_F}^{\rm nn.}$ refers to nearest-neighbor $\mathbf{k_F}$ from $\mathbf{k}$. This provides a local picture of the internal orbital structure of a pair which continues out to a radius set by the coherence length ξ_0. While implementing this extrapolation, one should keep in mind the translational invariance condition for the BZ, i.e, to obtain $\Delta_\mu(\mathbf{k})$ values in the 1^{st} BZ $(-\pi/a : \pi/a)$, contributions of $\Delta_\mu(\mathbf{k_F})$ values from the neighboring BZs $(-2\pi/a : 2\pi/a)$ should also be taken into account. The gap maxima value of $|\Delta_\mu(\mathbf{k})|$ in the BZ can also be set to a chosen Δ_0, for instance, 3.5 meV for our numerical purpose. The following describes the next steps of basis transformation from bands to orbital basis, for representing the gap (pairing) functions.

1. Tight-binding Hamiltonian

The non-interacting Hamiltonian $\hat{H}(\mathbf{k})$ as in Eq. (2) and (3), has the block diagonal structure:

$$\hat{H}(\mathbf{k}) = \begin{pmatrix} H_0(\mathbf{k}) + H_{\rm soc}(+) & 0 \\ 0 & H_0(\mathbf{k}) + H_{\rm soc}(-) \end{pmatrix}, \quad \text{(B2)}$$

Since $H_{\rm soc}(\sigma = \pm)$ has imaginary components, diagonalization of $\hat{H}(\mathbf{k})$ can yield eigenvectors that are linear combination of Kramer's degenerate eigenstates owing to gauge-independence. To circumvent this, one can diagonalize $H_+(\mathbf{k}) = H_0(\mathbf{k}) + H_{\rm soc}(+)$, and obtain the unitary matrix $U^{(+)}(\mathbf{k})$ and then $H_-(\mathbf{k}) = H_0(\mathbf{k}) + H_{\rm soc}(-)$, to obtain $U^{(-)}(\mathbf{k})$, and form the unitary matrix $U^{(0)}(\mathbf{k})$ such that:

$$U^{(0)}(\mathbf{k}) = \begin{pmatrix} U^{(+)}(\mathbf{k}) & 0 \\ 0 & U^{(-)}(\mathbf{k}) \end{pmatrix}, \quad \text{(B3)}$$

$$U^{(0)\dagger}(\mathbf{k})\hat{H}(\mathbf{k})U^{(0)}(\mathbf{k}) = \begin{pmatrix} E^{(+)}(\mathbf{k}) & 0 \\ 0 & E^{(-)}(\mathbf{k}) \end{pmatrix}, \quad \text{(B4)}$$

$U^{(0)}(\mathbf{k})$ diagonalizes $\hat{H}(\mathbf{k})$ to yield Kramer's degenerate pairs of eigenvalues $E^{(+)}(\mathbf{k}) = E^{(-)}(\mathbf{k})$.

2. Pairing function

The gap part of the BCS Hamiltonian $\hat{\Delta}(\mathbf{k})$ is constructed in the same basis as the $\hat{H}(\mathbf{k})$. However, the gap values obtained from Eq. (B1) are represented in band pseudospin basis. For the three bands present in the Sr_2RuO_4 system and for pseudospin-singlet pairing with the Cooper-pair structure: $|\uparrow\downarrow\rangle - |\downarrow\uparrow\rangle$, we construct the gap matrix in this band pseudospin basis as $\Delta^{\rm pseudo}(\mathbf{k})$:

$$\begin{pmatrix} . & . & . & \Delta_1(\mathbf{k}) & . & . \\ . & . & . & . & \Delta_2(\mathbf{k}) & . \\ . & . & . & . & . & -\Delta_3(\mathbf{k}) \\ -\Delta_1(\mathbf{k}) & . & . & . & . & . \\ . & -\Delta_2(\mathbf{k}) & . & . & . & . \\ . & . & \Delta_3(\mathbf{k}) & . & . & . \end{pmatrix}, \quad \text{(B5)}$$

where the pseudospin-structure of the basis is $(\uparrow,\uparrow,\downarrow,\downarrow,\downarrow,\uparrow)$. One constructs the gap part of the Hamiltonian in the Nambu basis as

$$\underline{\hat{H}}_\Delta = \begin{pmatrix} 0 & \Delta^{\rm pseudo}(\mathbf{k}) \\ \left(\Delta^{\rm pseudo}(\mathbf{k})\right)^\dagger & 0 \end{pmatrix}. \quad \text{(B6)}$$

The unitary matrix in this Nambu basis

$$\underline{U}_N(\mathbf{k}) = \begin{pmatrix} U^{(0)}(\mathbf{k}) & 0 \\ 0 & \left(U^{(0)}(-\mathbf{k})\right)^* \end{pmatrix}, \quad \text{(B7)}$$

that diagonalizes the non-interacting part of the Nambu Hamiltonian

$$\underline{\hat{H}}_N = \begin{pmatrix} \hat{H}(\mathbf{k}) & 0 \\ 0 & -\hat{H}^T(-\mathbf{k}) \end{pmatrix}, \quad \text{(B8)}$$

can be applied on $\underline{\hat{H}}_\Delta$ for unitary transformation from the band to orbital basis:

$$\underline{U}_N(\mathbf{k})\underline{\hat{H}}_\Delta(\mathbf{k})\underline{U}_N^\dagger(\mathbf{k}) = \begin{pmatrix} 0 & \hat{\Delta}(\mathbf{k}) \\ \hat{\Delta}^\dagger(\mathbf{k}) & 0 \end{pmatrix}. \quad \text{(B9)}$$

The matrix elements $\Delta_{mn}(\mathbf{k})$ of the block $\hat{\Delta}(\mathbf{k})$ are the orbitally resolved gap structure in the Nambu basis. Its real-space representation is obtained by a simple Fourier transformation:

$$\Delta_{mn}(\mathbf{R}) = \frac{1}{N_k}\sum_{\mathbf{k}} \Delta_{mn}(\mathbf{k}) e^{-i\mathbf{k}.\mathbf{R}}, \quad \text{(B10)}$$

where $\mathbf{R}$ refers to different lattice sites centered around (0,0). The amplitude $\Delta_{mn}(\mathbf{R})$ encodes the internal spatial and orbital structures of the electron pair. With the information of $\Delta_{mn}(\mathbf{R})$ and its simple inverse Fourier transformation back to momentum space, one can set up the full BCS Hamiltonian of Eq. (4) in combination with any tight-binding parameters.

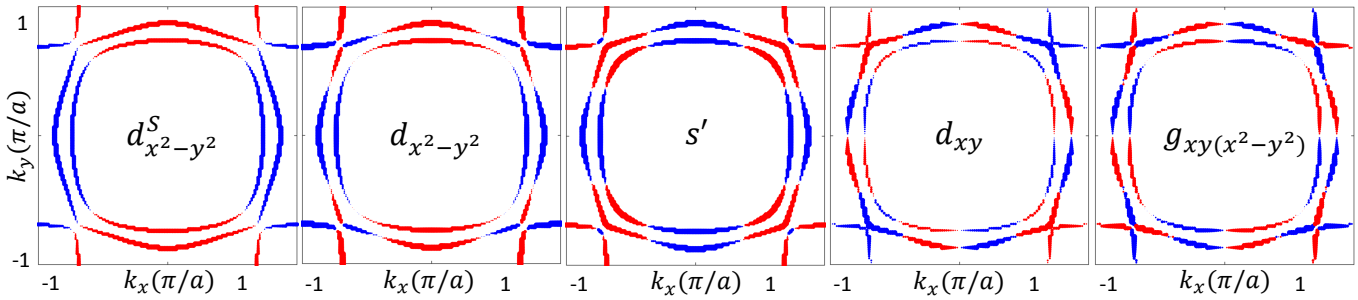

FIG. 6. Depictions of gap order parameters as a function of the Fermi surface for $d^S_{x^2-y^2}$ order parameter (simple intra-band form-factor of $\frac{\Delta_0}{2}(\cos k_x - \cos k_y)$), and the rest borrowed from Refs. 19 and 29 $d_{x^2-y^2}$, s', d_{xy} and $g_{xy(x^2-y^2)}$. The red (blue) color denotes positive (negative) values of the order parameter and marker-size of each $\mathbf{k_F}$ point is proportional to the gap magnitude $|\Delta(\mathbf{k_F})|$. Composite order parameters like $s' + id_{x^2-y^2}$, $s' + id_{xy}$ and $d_{x^2-y^2} + ig_{xy(x^2-y^2)}$ were obtained from complex combinations of the corresponding individual order parameters.

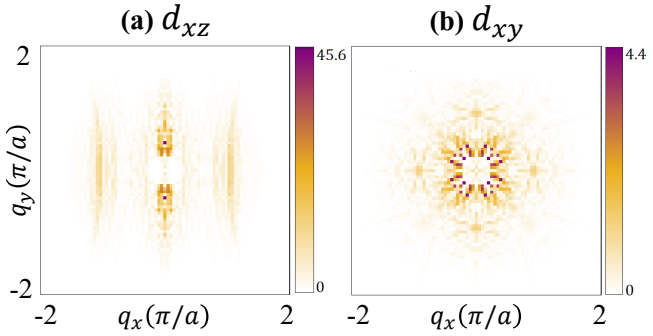

FIG. 7. Orbitally-resolved normal state QPI map for Sr_2RuO_4 at $\omega = 0$ for (a) d_{xz} and (b) d_{xy} orbitals. Notice that the QPI intensity magnitude are different for the two orbitals, with the d_{xy} orbital intensity being ~ 10 times weaker than the d_{xz} orbitals. The d_{yz}-orbital QPI map is same as in d_{xz}, but rotated by $\pi/2$.

Appendix C: Orbital contribution to the normal state QPI patterns

Here, we discuss the individual orbital contributions towards the normal state QPI pattern as shown in Fig. 7, evaluated as per the following equation for m-th orbital:

$$\rho_m(\mathbf{r},\omega) = -\frac{1}{\pi}\mathrm{Im}\sum_{\mathbf{R}\mathbf{R}'s}\hat{G}_{ms,ms}(\mathbf{R},\mathbf{R}',\omega)w_{\mathbf{R}m}(\mathbf{r})w_{\mathbf{R}'m}(\mathbf{r}) \tag{C1}$$

where $\hat{G}_{ms,ms}(\mathbf{R},\mathbf{R}',\omega)$ is the lattice Green's function in the presence of impurities (Eq. (7)) and $w_{\mathbf{R}m}(\mathbf{r})$ are the Wannier functions matrix elements. First, we attribute the double-cross feature seen in Fig. 2(b) to intra- and inter-band scattering between the d_{xz}/d_{yz}-dominated Fermi pockets in neighboring BZ. This can be verified from the d_{xz}-resolved QPI map in Fig. 7(a). These intraband scattering vectors have already been depicted in Fig. 2(a) by the green, blue and black arrows. We have not marked the interband scattering vectors, but they can be visualized as vectors connecting the d_{xz}-dominated parts of the β and the α pockets, closely aligned along the black arrow in Fig. 2(a). The less-intense $\mathbf{q}$-features along the diagonals of the BZ, correspond to the suppressed tunneling matrix elements for d_{xy} orbitals as shown in Fig. 7(b). One of these features is marked by the red arrow in Fig. 2(b). Notice that the $d_{xz}(= d_{yz})$ features are ~ 10 times stronger than the d_{xy} features. Note that the partial contribution to the density of states is given by the product of the lattice Green's function and the Wannier functions (see Eq.C1). To understand the difference in the intensities of the QPI maps, one needs to analyze the modulation of the lattice Green's function in conjunction with the Wannier wave functions. In Fig. 8, we show a $\log_{10}$-plot of the orbitally-resolved x, y-integrated ruthenium Wannier wave function amplitude as a function of the z-value of the unit cell representing Sr_2RuO_4. The integrated Wannier function amplitude is symmetric around the Ru atoms for both the orbitals, as expected. However, the $d_{xz}(= d_{yz})$ orbitals (yellow line) expand beyond the unit cell along the z-direction with a larger magnitude compared to the restricted spread of the d_{xy} orbitals (blue line). At a distance of 4.93Å above the surface, i.e. at $z = 13.93$Å, where we carry out our calculations, the $d_{xz}(= d_{yz})$ orbital integrated Wannier function amplitude is ~ 10 times stronger than the d_{xy} orbital. This ratio is exactly what we observe in the orbitally-resolved QPI intensity differences in Fig. 7. This difference between the orbital wave function intensity washes out most of the d_{xy} features and enhances the $d_{xz/yz}$ features in our BQPI maps.

Appendix D: Detailed description of the analysis of the BQPI patterns for ranking the different gap order parameters

In this section, we describe the score assignment procedure for ranking the different order parameters as per their BQPI pattern matching with the experiments. As mentioned earlier, we identified four $\mathbf{q}$-positions from

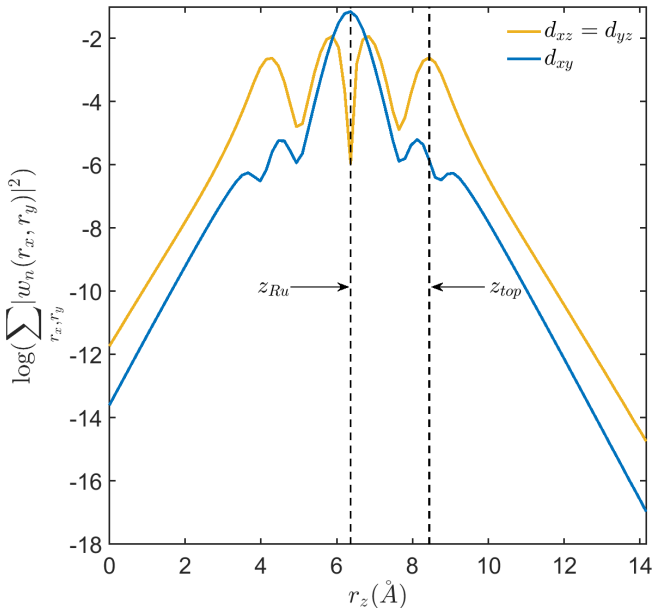

FIG. 8. A $\log_{10}$-plot of the orbitally-resolved x, y-integrated ruthenium Wannier wave function amplitude as a function of the z-value of the unit cell representing Sr_2RuO_4. The center of the unit cell containing the Ru atom has been marked by z_{Ru} in the figure. The top surface of the unit cell is denoted by z_{top}. The Wannier wave functions for the $d_{xz}(= d_{yz})$ orbitals (yellow line) expand beyond the unit cell along the z-direction with a larger magnitude compared to the restricted spread of the d_{xy} orbitals (blue line).

their ubiquitous and robust presence across all STM bias values in the experimental BQPI maps and marked them in red, green, blue and black colored circles (see Fig. 4, first row).

Next, we evaluate the integrated intensities of the BQPI maps around these four specific **q**-points, as a function of different STM bias values and for different order parameters along with the experimental data, as shown in Fig. 9. This was done by selecting a patch of 15×15 pixels centered at each colored circle. These intensities were normalized by the total integrated intensity over the full extended BZ at each STM bias for each order parameter. Next, we evaluate the mean-squared deviation (MSD) $\Delta y(j,i)$ of the integrated BQPI intensity between experimental and numerically evaluated BQPI maps for the 4 specific **q**-features centered inside the colored circles (i) for various gap order parameters (j). Table II quantifies the details of this analysis with rankings shown in descending order as before. The deviations are summed across all STM bias values. Since some **q**-points (example, red circle) tend to display a higher mean squared-deviation from the experimental counterpart than the other **q**-points, therefore, we assign a weight $\mathrm{w}(i)$ corresponding to each colored circle to reflect the nature of this discrepancy. To evaluate this weight $\mathrm{w}(i)$, first, we find the cumulative deviation corresponding to each colored circle across all order parameters. We pick the circle corresponding to the minimum of this cumulative deviation weight, i.e., the green point in this case. Next, we find normalized weights in units of this minimum cumulative weight by dividing the total weights by this minimum cumulative weight = 5.13 (written in bold in Table II). When we re-evaluate the weighted MSD $\overline{\Delta y(j)}$, we multiply the normalized weights $\overline{\mathrm{w}(i)}$ with the MSD $\Delta y(j,i)$ corresponding to each circle i for a specific order parameter j, to find the $\overline{\Delta y(j)}$. This $\overline{\Delta y(j)}$ score determines the ranking for the correspondence of the individual gap order parameters when matched with experimental BQPI patterns:

$$\overline{\Delta y(j)} = \sum_{\text{point } i=1,2,3,4} \Delta y(j,i)\ \ \overline{\mathrm{w}(i)} \qquad \text{(D1)}$$

as provided in Table I in the main text. An additional experimental feature is the enhanced intensities along the square edges positioned around $(\pm 1.5\pi/a)$ at higher STM biases $|\omega|/\Delta = [0.58, 0.84]$ as opposed to the lower biases $|\omega|/\Delta = [0, 0.26]$. We observe that the $s' + id_{xy}$ order parameter also displays a similar trend in its BQPI map, while other order parameters display different trends. Our approach is based on the choice of dominant **q**-features and results might change if different choices were made. Unfortunately, we do not have a more robust way to approach this pattern-matching problem. We are restricted by the limited availability of experimental data at ultra-low temperatures.

MSD $\Delta y(j,i)$ from exp. intensity data				
Gap order	Red point	Blue point	Green point	Black point
$s'+id_{x^2-y^2}$	6.12	1.81	0.74	0.98
$d_{x^2-y^2}$	4.63	1.70	0.82	1.94
$d^S_{x^2-y^2}$	3.45	1.31	0.62	3.72
$d_{x^2-y^2} + ig_{xy(x^2-y^2)}$	4.37	3.41	1.72	4.42
s'	6.13	2.24	0.68	0.65
$s' + id_{xy}$	5.99	1.15	0.55	1.93
Total $\mathrm{w}(i)$	30.69	11.62	**5.13**	13.64
Normalized $\overline{\mathrm{w}(i)}$	0.17	0.44	1.0	0.38

TABLE II. Table displaying the mean-squared deviation $\Delta y(j,i)$ of the integrated BQPI intensity between experimental and numerically evaluated BQPI maps, around the four specific **q**-features at the colored circles (i) (see Fig. 4) for various gap order parameters (j). The last two rows show the summed total weights $\mathrm{w}(i)$ and the normalized weights $\overline{\mathrm{w}(i)}$, as described in the text above in Appendix D.

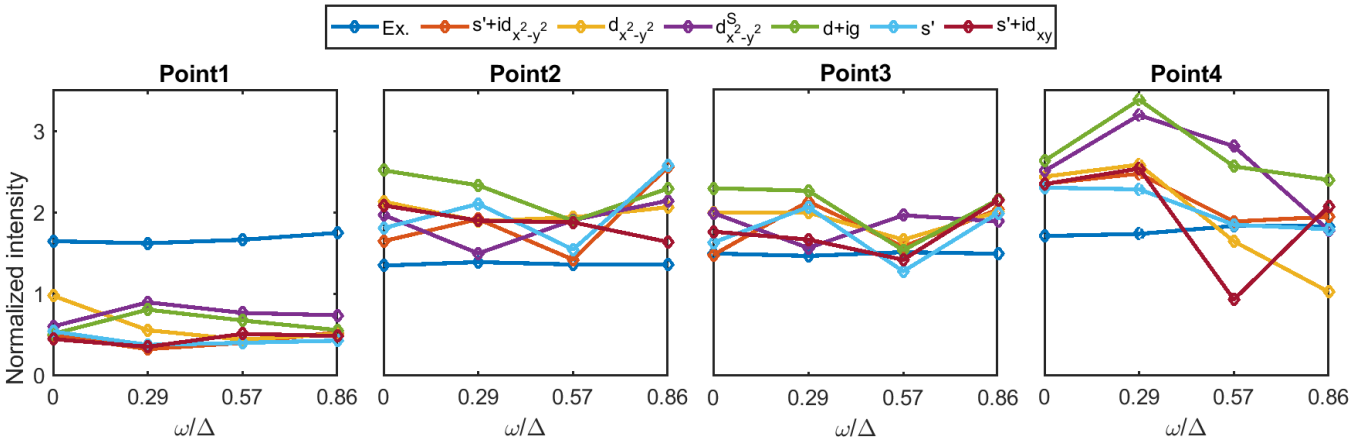

FIG. 9. Left to right: Normalized integrated intensities around each **q**-point, encircled in red (point 1), blue (point 2), green (point 3) and black (point 4) colors in Fig. 4, as a function of STM bias values ω/Δ, for different gap order parameters as indicated by the legend on top. The normalization was done with respect to the fully integrated BQPI intensity over the extended BZ at each bias value for each order parameter.

[1] Andrew Peter Mackenzie and Yoshiteru Maeno, "The superconductivity of Sr_2RuO_4 and the physics of spin-triplet pairing," Rev. Mod. Phys. **75**, 657–712 (2003).

[2] Yoshiteru Maeno, Shunichiro Kittaka, Takuji Nomura, Shingo Yonezawa, and Kenji Ishida, "Evaluation of spin-triplet superconductivity in Sr_2RuO_4," Journal of the Physical Society of Japan **81**, 011009 (2012).

[3] Catherine Kallin and John Berlinsky, "Chiral superconductors," Reports on Progress in Physics **79**, 054502 (2016).

[4] Andrew P. Mackenzie, Thomas Scaffidi, Clifford W. Hicks, and Yoshiteru Maeno, "Even odder after twenty-three years: the superconducting order parameter puzzle of Sr_2RuO_4," npj Quantum Materials **2** (2017).

[5] K. Ishida, H. Mukuda, Y. Kitaoka, K. Asayama, Z. Q. Mao, Y. Mori, and Y. Maeno, "Spin-triplet superconductivity in Sr_2RuO_4 identified by 17o Knight shift," Nature **396**, 658–660 (1998).

[6] G. M. Luke, Y. Fudamoto, K. M. Kojima, M. I. Larkin, J. Merrin, B. Nachumi, Y. J. Uemura, Y. Maeno, Z. Q. Mao, Y. Mori, H. Nakamura, and M. Sigrist, "Time-reversal symmetry-breaking superconductivity in Sr_2RuO_4," Nature **394**, 558–561 (1998).

[7] Jing Xia, Yoshiteru Maeno, Peter T. Beyersdorf, M. M. Fejer, and Aharon Kapitulnik, "High resolution polar kerr effect measurements of Sr_2RuO_4: Evidence for broken time-reversal symmetry in the superconducting state," Phys. Rev. Lett. **97**, 167002 (2006).

[8] T M Rice and M Sigrist, "Sr_2RuO_4: an electronic analogue of 3He?" Journal of Physics: Condensed Matter **7**, L643–L648 (1995).

[9] I. Bonalde, Brian D. Yanoff, M. B. Salamon, D. J. Van Harlingen, E. M. E. Chia, Z. Q. Mao, and Y. Maeno, "Temperature dependence of the penetration depth in Sr_2RuO_4: Evidence for nodes in the gap function," Phys. Rev. Lett. **85**, 4775–4778 (2000).

[10] Shuji NishiZaki, Yoshiteru Maeno, and Zhiqiang Mao, "Changes in the superconducting state of Sr_2RuO_4 under magnetic fields probed by specific heat," Journal of the Physical Society of Japan **69**, 572–578 (2000).

[11] K. Deguchi, Z. Q. Mao, H. Yaguchi, and Y. Maeno, "Gap structure of the spin-triplet superconductor Sr_2RuO_4 determined from the field-orientation dependence of the specific heat," Phys. Rev. Lett. **92**, 047002 (2004).

[12] E. Hassinger, P. Bourgeois-Hope, H. Taniguchi, S. René de Cotret, G. Grissonnanche, M. S. Anwar, Y. Maeno, N. Doiron-Leyraud, and Louis Taillefer, "Vertical line nodes in the superconducting gap structure of Sr_2RuO_4," Phys. Rev. X **7**, 011032 (2017).

[13] A. Pustogow, Yongkang Luo, A. Chronister, Y.-S. Su, D. A. Sokolov, F. Jerzembeck, A. P. Mackenzie, C. W. Hicks, N. Kikugawa, S. Raghu, and et al., "Constraints on the superconducting order parameter in Sr_2RuO_4 from oxygen-17 nuclear magnetic resonance," Nature **574**, 72–75 (2019).

[14] Kenji Ishida, Masahiro Manago, Katsuki Kinjo, and Yoshiteru Maeno, "Reduction of the ^{17}O Knight Shift in the Superconducting State and the Heat-up Effect by NMR Pulses on Sr_2RuO_4," Journal of the Physical Society of Japan **89**, 034712 (2020).

[15] Aaron Chronister, Andrej Pustogow, Naoki Kikugawa, Dmitry A. Sokolov, Fabian Jerzembeck, Clifford W. Hicks, Andrew P. Mackenzie, Eric D. Bauer, and Stuart E. Brown, "Evidence for even parity unconventional superconductivity in Sr_2RuO_4," Proceedings of the National Academy of Sciences **118** (2021).

[16] S. Benhabib, C. Lupien, I. Paul, L. Berges, M. Dion, M. Nardone, A. Zitouni, Z. Q. Mao, Y. Maeno, A. Georges, and et al., "Ultrasound evidence for a two-component superconducting order parameter in Sr_2RuO_4," Nature Physics **17**, 194–198 (2020).

[17] Sayak Ghosh, Arkady Shekhter, F. Jerzembeck, N. Kikugawa, Dmitry A. Sokolov, Manuel Brando, A. P. Mackenzie, Clifford W. Hicks, and B. J. Ramshaw, "Thermodynamic evidence for a two-component superconducting order parameter in Sr_2RuO_4," Nature Physics **17**, 199–204 (2020).

[18] Vadim Grinenko, Shreenanda Ghosh, Rajib Sarkar, Jean-Christophe Orain, Artem Nikitin, Matthias Elender, Debarchan Das, Zurab Guguchia, Felix Brückner, Mark E. Barber, Joonbum Park, Naoki Kikugawa, Dmitry A. Sokolov, Jake S. Bobowski, Takuto Miyoshi, Yoshiteru Maeno, Andrew P. Mackenzie, Hubertus Luetkens, Clifford W. Hicks, and Hans-Henning Klauss, "Split superconducting and time-reversal symmetry-breaking transitions in Sr_2RuO_4 under stress," Nature Physics **17**, 748–754 (2021).

[19] A. T. Rømer, D. D. Scherer, I. M. Eremin, P. J. Hirschfeld, and B. M. Andersen, "Knight shift and leading superconducting instability from spin fluctuations in Sr_2RuO_4," Phys. Rev. Lett. **123**, 247001 (2019).

[20] Henrik S. Røising, Thomas Scaffidi, Felix Flicker, Gunnar F. Lange, and Steven H. Simon, "Superconducting order of Sr_2RuO_4 from a three-dimensional microscopic model," Phys. Rev. Research **1**, 033108 (2019).

[21] O. Gingras, R. Nourafkan, A.-M. S. Tremblay, and M. Côté, "Superconducting symmetries of Sr_2RuO_4 from first-principles electronic structure," Phys. Rev. Lett. **123**, 217005 (2019).

[22] Han Gyeol Suh, Henri Menke, P. M. R. Brydon, Carsten Timm, Aline Ramires, and Daniel F. Agterberg, "Stabilizing even-parity chiral superconductivity in Sr_2RuO_4," Phys. Rev. Research **2**, 032023 (2020).

[23] S.-O. Kaba and D. Sénéchal, "Group-theoretical classification of superconducting states of strontium ruthenate," Phys. Rev. B **100**, 214507 (2019).

[24] Aline Ramires and Manfred Sigrist, "Superconducting order parameter of Sr_2RuO_4: A microscopic perspective," Phys. Rev. B **100**, 104501 (2019).

[25] Swagata Acharya, Dimitar Pashov, Cédric Weber, Hyowon Park, Lorenzo Sponza, and Mark Van Schilfgaarde, "Evening out the spin and charge parity to increase T_c in Sr_2RuO_4," Communications Physics **2**, 163 (2019).

[26] Zhiqiang Wang, Xin Wang, and Catherine Kallin, "Spin-orbit coupling and spin-triplet pairing symmetry in Sr_2RuO_4," Phys. Rev. B **101**, 064507 (2020).

[27] Astrid T. Rømer, Andreas Kreisel, Marvin A. Müller, P. J. Hirschfeld, Ilya M. Eremin, and Brian M. Andersen, "Theory of strain-induced magnetic order and splitting of T_c and T_{trsb} in Sr_2RuO_4," Phys. Rev. B **102** (2020).

[28] A. T. Rømer and B. M. Andersen, "Fluctuation-driven superconductivity in Sr_2RuO_4 from weak repulsive interactions," Modern Physics Letters B **34**, 2040052 (2020).

[29] Astrid T. Rømer, P. J. Hirschfeld, and Brian M. Andersen, "Superconducting state of Sr_2RuO_4 in the presence of longer-range Coulomb interactions," Phys. Rev. B **104**, 064507 (2021).

[30] Steven Allan Kivelson, Andrew Chang Yuan, Brad Ramshaw, and Ronny Thomale, "A proposal for reconciling diverse experiments on the superconducting state in Sr_2RuO_4," npj Quantum Materials **5** (2020).

[31] Jonathan Clepkens, Austin W. Lindquist, and Hae-Young Kee, "Shadowed triplet pairings in Hund's metals with spin-orbit coupling," Phys. Rev. Research **3**, 013001 (2021).

[32] Roland Willa, Matthias Hecker, Rafael M. Fernandes, and Jörg Schmalian, "Inhomogeneous time-reversal symmetry breaking in Sr_2RuO_4," Phys. Rev. B **104**, 024511 (2021).

[33] Astrid T. Rømer, T. A. Maier, Andreas Kreisel, P. J. Hirschfeld, and Brian M. Andersen, "Leading superconducting instabilities in three-dimensional models for Sr_2RuO_4," Phys. Rev. Res. **4**, 033011 (2022).

[34] Mercè Roig, Astrid T. Rømer, Andreas Kreisel, P. J. Hirschfeld, and Brian M. Andersen, "Superconductivity in multiorbital systems with repulsive interactions: Hund's pairing versus spin-fluctuation pairing," Phys. Rev. B **106**, L100501 (2022).

[35] Henrik S. Røising, Glenn Wagner, Mercè Roig, Astrid T. Rømer, and Brian M. Andersen, "Heat capacity double transitions in time-reversal symmetry broken superconductors," Phys. Rev. B **106**, 174518 (2022).

[36] Fabian B. Kugler, Manuel Zingl, Hugo U. R. Strand, Seung-Sup B. Lee, Jan von Delft, and Antoine Georges, "Strongly correlated materials from a numerical renormalization group perspective: How the Fermi-liquid state of Sr_2RuO_4 emerges," Phys. Rev. Lett. **124**, 016401 (2020).

[37] Jernej Mravlje, Markus Aichhorn, Takashi Miyake, Kristjan Haule, Gabriel Kotliar, and Antoine Georges, "Coherence-Incoherence Crossover and the Mass-Renormalization Puzzles in Sr_2RuO_4," Phys. Rev. Lett. **106**, 096401 (2011).

[38] M. W. Haverkort, I. S. Elfimov, L. H. Tjeng, G. A. Sawatzky, and A. Damascelli, "Strong spin-orbit coupling effects on the Fermi surface of Sr_2RuO_4 and Sr_2RhO_4," Phys. Rev. Lett. **101**, 026406 (2008).

[39] Minjae Kim, Jernej Mravlje, Michel Ferrero, Olivier Parcollet, and Antoine Georges, "Spin-orbit coupling and electronic correlations in Sr_2RuO_4," Phys. Rev. Lett. **120**, 126401 (2018).

[40] S. Raghu, A. Kapitulnik, and S. A. Kivelson, "Hidden quasi-one-dimensional superconductivity in Sr_2RuO_4," Phys. Rev. Lett. **105**, 136401 (2010).

[41] Thomas Scaffidi, Jesper C. Romers, and Steven H. Simon, "Pairing symmetry and dominant band in Sr_2RuO_4," Phys. Rev. B **89**, 220510 (2014).

[42] S. Benhabib, C. Lupien, I. Paul, L. Berges, M. Dion, M. Nardone, A. Zitouni, Z. Q. Mao, Y. Maeno, A. Georges, L. Taillefer, and C. Proust, "Ultrasound evidence for a two-component superconducting order parameter in Sr_2RuO_4," Nature Physics **17**, 194–198 (2021).

[43] I. A. Firmo, S. Lederer, C. Lupien, A. P. Mackenzie, J. C. Davis, and S. A. Kivelson, "Evidence from tunneling spectroscopy for a quasi-one-dimensional origin of superconductivity in Sr_2RuO_4," Phys. Rev. B **88**, 134521 (2013).

[44] Rahul Sharma, Stephen D. Edkins, Zhenyu Wang, Andrey Kostin, Chanchal Sow, Yoshiteru Maeno, Andrew P. Mackenzie, J. C. Séamus Davis, and Vidya Madhavan, "Momentum-resolved superconducting energy gaps of Sr_2RuO_4 from quasiparticle interference imaging," Proceedings of the National Academy of Sciences **117**, 5222–5227 (2020).

[45] Tamara S. Nunner, Wei Chen, Brian M. Andersen, Ashot Melikyan, and P. J. Hirschfeld, "Fourier transform spectroscopy of d-wave quasiparticles in the presence of atomic scale pairing disorder," Phys. Rev. B **73**, 104511 (2006).

[46] T. Hanaguri, Y. Kohsaka, J. C. Davis, C. Lupien, I. Yamada, M. Azuma, M. Takano, K. Ohishi, M. Ono, and H. Takagi, "Quasiparticle interference and superconducting gap in $Ca_{2-x}Na_xCuO_2Cl_2$," Nature Physics **3**, 865–871 (2007).

[47] M. P. Allan, A. W. Rost, A. P. Mackenzie, Yang Xie, J. C. Davis, K. Kihou, C. H. Lee, A. Iyo, H. Eisaki, and T.-M. Chuang, "Anisotropic energy gaps of iron-based superconductivity from intraband quasiparticle interference in LiFeAs," Science **336**, 563–567 (2012).

[48] P. O. Sprau, A. Kostin, A. Kreisel, A. E. Böhmer, V. Taufour, P. C. Canfield, S. Mukherjee, P. J. Hirschfeld, B. M. Andersen, and J. C. Séamus Davis, "Discovery of orbital-selective cooper pairing in FeSe," Science **357**, 75–80 (2017).

[49] Satoshi Kashiwaya, Kohta Saitoh, Hiromi Kashiwaya, Masao Koyanagi, Masatoshi Sato, Keiji Yada, Yukio Tanaka, and Yoshiteru Maeno, "Time-reversal invariant superconductivity of Sr_2RuO_4 revealed by josephson effects," Phys. Rev. B **100**, 094530 (2019).

[50] A. Kreisel, Peayush Choubey, T. Berlijn, W. Ku, B. M. Andersen, and P. J. Hirschfeld, "Interpretation of scanning tunneling quasiparticle interference and impurity states in cuprates," Phys. Rev. Lett. **114**, 217002 (2015).

[51] A. Kreisel, R. Nelson, T. Berlijn, W. Ku, Ramakrishna Aluru, Shun Chi, Haibiao Zhou, Udai Raj Singh, Peter Wahl, Ruixing Liang, Walter N. Hardy, D. A. Bonn, P. J. Hirschfeld, and Brian M. Andersen, "Towards a quantitative description of tunneling conductance of superconductors: Application to LiFeAs," Phys. Rev. B **94**, 224518 (2016).

[52] V.B. Zabolotnyy, D.V. Evtushinsky, A.A. Kordyuk, T.K. Kim, E. Carleschi, B.P. Doyle, R. Fittipaldi, M. Cuoco, A. Vecchione, and S.V. Borisenko, "Renormalized band structure of Sr_2RuO_4: A quasiparticle tight-binding approach," Journal of Electron Spectroscopy and Related Phenomena **191**, 48–53 (2013).

[53] Sergio Cobo, Felix Ahn, Ilya Eremin, and Alireza Akbari, "Anisotropic spin fluctuations in Sr_2RuO_4 : Role of spin-orbit coupling and induced strain," Phys. Rev. B **94** (2016).

[54] Jennifer E Hoffman, "Spectroscopic scanning tunneling microscopy insights into fe-based superconductors," Reports on Progress in Physics **74**, 124513 (2011).

[55] A. Kreisel, C. A. Marques, L. C. Rhodes, X. Kong, T. Berlijn, R. Fittipaldi, V. Granata, A. Vecchione, P. Wahl, and P. J. Hirschfeld, "Quasi-particle interference of the van Hove singularity in Sr2RuO4," npj Quantum Materials **6**, 100 (2021).

[56] I. A. Firmo, S. Lederer, C. Lupien, A. P. Mackenzie, J. C. Davis, and S. A. Kivelson, "Evidence from tunneling spectroscopy for a quasi-one-dimensional origin of superconductivity in Sr_2RuO_4," Phys. Rev. B **88**, 134521 (2013).

[57] Hiroki Tsuchiura, Yukio Tanaka, Masao Ogata, and Satoshi Kashiwaya, "Local magnetic moments around a nonmagnetic impurity in the two-dimensional $t-J$ model," Phys. Rev. B **64**, 140501 (2001).

[58] Ziqiang Wang and Patrick A. Lee, "Local Moment Formation in the Superconducting State of a Doped Mott Insulator," Phys. Rev. Lett. **89**, 217002 (2002).

[59] Jian-Xin Zhu, Ivar Martin, and A. R. Bishop, "Spin and Charge Order around Vortices and Impurities in High-T_c Superconductors," Phys. Rev. Lett. **89**, 067003 (2002).

[60] Yan Chen and C. S. Ting, "States of Local Moment Induced by Nonmagnetic Impurities in Cuprate Superconductors," Phys. Rev. Lett. **92**, 077203 (2004).

[61] Brian M. Andersen, P. J. Hirschfeld, Arno P. Kampf, and Markus Schmid, "Disorder-Induced Static Antiferromagnetism in Cuprate Superconductors," Phys. Rev. Lett. **99**, 147002 (2007).

[62] J. W. Harter, B. M. Andersen, J. Bobroff, M. Gabay, and P. J. Hirschfeld, "Antiferromagnetic correlations and impurity broadening of NMR linewidths in cuprate superconductors," Phys. Rev. B **75**, 054520 (2007).

[63] Brian M. Andersen, Siegfried Graser, and P. J. Hirschfeld, "Disorder-Induced Freezing of Dynamical Spin Fluctuations in Underdoped Cuprate Superconductors," Phys. Rev. Lett. **105**, 147002 (2010).

[64] Markus Schmid, Brian M Andersen, Arno P Kampf, and P J Hirschfeld, "d-Wave superconductivity as a catalyst for antiferromagnetism in underdoped cuprates," New Journal of Physics **12**, 053043 (2010).

[65] Maria N. Gastiasoro, P. J. Hirschfeld, and Brian M. Andersen, "Impurity states and cooperative magnetic order in Fe-based superconductors," Phys. Rev. B **88**, 220509 (2013).

[66] Bastian Zinkl and Manfred Sigrist, "Impurity-induced magnetic ordering in Sr_2RuO_4," Phys. Rev. Research **3**, 023067 (2021).

[67] Zhenyu Wang, Daniel Walkup, Philip Derry, Thomas Scaffidi, Melinda Rak, Sean Vig, Anshul Kogar, Ilija Zeljkovic, Ali Husain, Luiz H. Santos, and et al., "Quasiparticle interference and strong electron-mode coupling in the quasi-one-dimensional bands of Sr_2RuO_4," Nature Physics **13**, 799–805 (2017).

[68] K. McElroy, R. W. Simmonds, J. E. Hoffman, D. H. Lee, J. Orenstein, H. Eisaki, S. Uchida, and J. C. Davis, "Relating atomic-scale electronic phenomena to wave-like quasiparticle states in superconducting $Bi_2Sr_2CaCu_2O_{8+\delta}$," Nature **422**, 592–596 (2003).

[69] Yi Zhang, A. Mesaros, K. Fujita, S. D. Edkins, M. H. Hamidian, K. Ch'ng, H. Eisaki, S. Uchida, J. C. Séamus Davis, Ehsan Khatami, and Eun-Ah Kim, "Machine learning in electronic-quantum-matter imaging experiments," Nature **570**, 484–490 (2019).

[70] G. Kresse and J. Furthmüller, "Efficient iterative schemes for ab initio total-energy calculations using a plane-wave basis set," Phys. Rev. B **54**, 11169–11186 (1996).

[71] G. Kresse and D. Joubert, "From ultrasoft pseudopotentials to the projector augmented-wave method," Phys. Rev. B **59**, 1758–1775 (1999).

[72] John P. Perdew, Kieron Burke, and Matthias Ernzerhof, "Generalized gradient approximation made simple," Phys. Rev. Lett. **77**, 3865–3868 (1996).

[73] Arash A. Mostofi, Jonathan R. Yates, Young-Su Lee, Ivo Souza, David Vanderbilt, and Nicola Marzari, "Wannier90: A tool for obtaining maximally-localised Wannier functions," Computer Physics Communications **178**, 685–699 (2008).